MULTISCALE MODEL. SIMUL.
Vol. 6, No. 3, pp. 858–878

© 2007 Society for Industrial and Applied Mathematics

MICROSCOPIC-MACROSCOPIC SIMULATIONS OF RIGID-ROD POLYMER HYDRODYNAMICS: HETEROGENEITY AND RHEOCHAOS*

M. GREGORY FOREST[†], RUHAI ZHOU[‡], AND QI WANG[§]

Abstract. Rheochaos is a remarkable phenomenon of nematic (rigid-rod) polymers in steady shear, with sustained chaotic fluctuations of the orientational distribution of the rod ensemble. For monodomain dynamics, imposing spatial homogeneity and linear shear, rheochaos is a hallmark prediction of the Doi–Hess theory [M. Doi, *J. Polym. Sci. Polym. Phys. Ed.*, 19 (1981), pp. 229–243; M. Doi and S. F. Edwards, *The Theory of Polymer Dynamics*, Oxford University Press, London, New York, 1986; S. Hess, *Z. Naturforsch.*, 31 (1976), pp. 1034–1037]. The model behavior is robust, captured by second-moment tensor approximations [G. Rienäcker, M. Kröger, and S. Hess, *Phys. Rev. E* (3), 66 (2002), 040702; G. Rienäcker, M. Kröger, and S. Hess, *Phys. A*, 315 (2002), pp. 537–568; M. G. Forest and Q. Wang, *Rheol. Acta*, 42 (2003), pp. 20–46] and high-order Galerkin simulations of the Smoluchowski equation for the orientational probability distribution function (PDF) [M. Grosso, R. Keunings, S. Crescitelli, and P. L. Maffettone, *Phys. Rev. Lett.*, 86 (2001), pp. 3184–3187; M. G. Forest, Q. Wang, and R. Zhou, *Rheol. Acta*, 43 (2004), pp. 17–37; M. G. Forest, Q. Wang, and R. Zhou, *Rheol. Acta*, 44 (2004), pp. 80–93], and persistent up to critical thresholds of coplanar extensional flow [M. G. Forest, R. Zhou, and Q. Wang, *Phys. Rev. Lett.*, 93 (2004), 088301; M. G. Forest, Q. Wang, R. Zhou, and E. Choate, *J. Non-Newt. Fluid Mech.*, 118 (2004), pp. 17–31; S. Heidenreich, P. Ilg, and S. Hess, *Phys. Rev. E* (3), 73 (2006), 061710] and magnetic fields [M. G. Forest, Q. Wang, H. Zhou, and R. Zhou, *J. Rheol.*, 48 (2004), pp. 175–192], as well as fluctuating shear rates [S. Heidenreich, P. Ilg, and S. Hess, *Phys. Rev. E* (3), 73 (2006), 061710]. To be experimentally relevant, rheochaos of the Doi–Hess theory must persist amid heterogeneity observed in birefringence patterns [Z. Tan and G. C. Berry, *J. Rheol.*, 47 (2003), pp. 73–104]. Modeling can further shed light on shear bands produced by hydrodynamic feedback which have thus far eluded measurement. Some numerical evidence supports persistence: a one-dimensional (1D) study [B. Chakrabarti, M. Das, C. Dasgupta, S. Ramaswamy, and A. K. Sood, *Phys. Rev. Lett.*, 92 (2004), 188301] with a second-moment tensor model and imposed simple shear; and a two-dimensional (2D) study [A. Furukawa and A. Onuki, *Phys. D*, 205 (2005), pp. 195–206] with a second-moment tensor model and flow feedback. Here we stage the micro-macro (Smoluchowski and Navier–Stokes) system so that monodomain rheochaos is embedded in a 1D simulation [R. Zhou, M. G. Forest, and Q. Wang, *Multiscale Model. Simul.*, 3 (2005), pp. 853–870] of a planar shear cell experiment with distortional elasticity. Longtime simulations reveal (i) heterogeneous rheochaos marked by chaotic time series in the PDF, normal and shear stresses, and velocity field at each interior gap height; (ii) coherent spatial morphology in the PDF and stress profiles across the shear gap and weakly nonlinear shear bands in each snapshot; and (iii) consistency between heterogeneous and monodomain rheochaos as measured by Lyapunov exponents and pointwise orbits of the peak orientation of the PDF but with enhancement rather than reduction in Lyapunov exponent values in the flow coupled, heterogeneous system.

Key words. spatialtemporal chaos, nematic polymer, hydrodynamics

AMS subject classifications. 76A05, 76E30

DOI. 10.1137/070681491

---

*Received by the editors January 25, 2007; accepted for publication (in revised form) April 24, 2007; published electronically September 12, 2007. This work was supported by AFOSR grants FA9550-05-1-0025 and FA9550-06-1-0063, NSF grants DMS-0604891, DMS-0604912, DMS-0605029, and DMS-0626180, NASA URETI BIMat award NCC-1-02037, and the Army Research Office.

http://www.siam.org/journals/mms/6-3/68149.html

[†] Department of Mathematics, Institute for Advanced Materials, Nanoscience and Technology, University of North Carolina, Chapel Hill, NC 27599-3250 (forest@amath.unc.edu).

[‡] Department of Mathematics and Statistics, Old Dominion University, Norfolk, VA 23529 (rzhou@odu.edu). This author was partially supported by Old Dominion University Research Foundation Summer Research Fellowship Program 2006.

[§] Department of Mathematical Sciences, Florida State University, Tallahassee, FL 32306 (wang@math.fsu.edu).

Copyright © by SIAM. Unauthorized reproduction of this article is prohibited.

1. Introduction and motivation.

There is a preponderance of experimental and modeling evidence for sustained fluctuations of soft microstructural phases during steady shear experiments in complex fluids. These soft microphases include wormlike micelles and surfactant solutions, where shear banding through hydrodynamic feedback has been extensively investigated [49, 5, 4, 15, 14, 29, 1, 2, 3, 36, 47, 37, 45, 46, 59].

Some of these studies report apparent chaotic fluctuations associated with the sheared microstructural phases. This behavior in sheared nematic polymers is the focus of the present paper, where there is convincing experimental evidence for irregular stress fluctuations and complex birefringence patterns in steady shear; see the review by Tan and Berry [55]. The phenomenon of chaotic orientational dynamics is reproduced numerically from the Doi–Hess theory [9, 10, 35] of sheared nematic polymer monodomains, both with resolved kinetic simulations [30, 20, 21] and with second-moment tensor reduced models [52, 51, 18]. These predictions persist over a remarkable range of physical parametrizations, including coupled extension-shear flows that are shear dominated [24], a finite range of rod volume fractions, and in coupled coplanar magnetic fields [17, 22].

The question that motivates this study is whether monodomain rheochaos of the Doi–Hess theory [35, 9, 10] persists when two new physical features are coupled: the nematic liquid is confined between moving plates (where the liquid must satisfy boundary anchoring constraints on the orientational distribution), and hydrodynamic feedback through orientational stress gradients is coupled. With homogeneous initial data, the numerical experiment poses a spatial conflict between the interior nematic liquid which is prone to chaotic oscillations for a range of plate speeds, whereas the orientation is stationary at the walls. Spatial gradients in the orientational distribution are spawned across the plate gap, which generates nonlinearity in the flow field through the elastic stress, additional orientational gradients are generated, and so on. At issue is how the spatial and temporal features of the flow and orientational distribution saturate, i.e., the longtime attractor of the system. The distortional elasticity potential of Marrucci and Greco (cf. [58, 64, 25]) is coupled with the Smoluchowski and Navier–Stokes system for this purpose.

Rigid-rod macromolecules in a viscous solvent present ideal model systems to explore complex nonlinear phenomena of anisotropic viscoelasticity. In particular, there is a solid theoretical foundation for a multiscale coupling of the macroscopic flow field and the microscopic dynamics of the rod ensemble. We begin from the numerical basis where the longwave dynamics is fairly well under control, with detailed studies of shear-induced rheochaos of the orientational distribution when the flow is imposed. The emergence of new length-scale structures between the molecular and device scales remains relatively unknown, with significant studies in parameter regimes where the attractors are either steady or regular [57, 42, 13, 12, 39, 64, 25]. These numerical studies rely upon the molecular physics theoretical foundation provided by Hess [35], Doi [9], and Doi and Edwards [10] for the orientational probability distribution function (PDF) of the rod ensemble and then Landau–de Gennes second-moment approximate models. Gradient morphology and hydrodynamic feedback are coupled through the distortional elasticity potential of Marrucci and Greco [48]. This system reduces to Frank elasticity for liquid crystals in the small molecule, weak flow limit [58], providing a baseline of comparison with the liquid crystal literature of the past three decades. Another kinetic scale approach has been developed by Kröger and Ilg [41], wherein they recover all Frank elastic coefficients by incorporating effects of translational diffusion; the final chapter on the upscaling from a mean-field

Copyright © by SIAM. Unauthorized reproduction of this article is prohibited.

kinetic theory to a mesoscopic theory remains to be written. The key extension of the Doi–Hess–Marrucci–Greco theory beyond the Leslie–Ericksen–Frank theory is in the self-consistent coupling of short-range excluded volume interactions and in the kinetic description of the PDF whose peak axis of orientation yields the coarse-grained liquid crystal director. Several other groups (cf. the works of Rey, Leal, Feng, Denn and collaborators, and more recently Helzel and Otto, Klein and Garcia-Cervera, et al., and Zhang's group at Peking University) have built numerical codes for the hydrodynamics of nematic polymers in shear cells [56, 42, 53, 34, 39, 60].

Our purpose here is not to explore the diversity of space-time attractors, nor is it to explore a wide range of parameter space. Rather, our purpose is to highlight behavior in the parameter regime of the Doi–Hess–Marrucci–Greco model where monodomain rheochaos couples with anchoring-induced gradient morphology and to explore whether spatial degrees of freedom and flow feedback are sufficient to arrest the chaotic orbits of the decoupled Smoluchowski equation. From detailed studies of monodomain phase diagrams [20, 24, 23] and the robustness of regular and chaotic orbits to imposed shear rate fluctuations [33], there is reason to anticipate robustness of erratic orientational dynamics in the presence of local spatial variations in shear rate. But these results, while suggestive, are within the one-way coupling in which an imposed linear flow drives the Smoluchowski dynamics of the rod ensemble, without spatial gradients or hydrodynamic feedback. Since we discretize space with a finite difference method, one can make the analogy of our numerical model with a "Smoluchowski chain," consisting of a finite chain of Smoluchowski oscillators which are coupled both with one another through the elasticity potential and with the driven fluid bath in which they reside.

With this backdrop, we design simulations to investigate how chaotic longwave dynamics injects energy from plate motion into morphology of the molecular orientational distribution, stored stresses, and flow (shear banding) and how this space-time model system saturates after sufficiently long times. We are interested in whether spatial degrees of freedom are sufficient to arrest the chaotic time series of the PDF and, if not, whether the flow inherits the chaotic dynamics; second, we are interested in whether the spatial degrees of freedom are localized in "coherent structures" or broad-banded (and thereby also chaotic).

A strained analogy exists with the theoretical and experimental work on sheared wormlike micellar solutions [5, 28, 50, 4, 16, 14, 44], where order-disorder transitions of the micelles correlate with nonlinear shear banding. The micelles are analogous to the local (micron-size) monodomains of rod ensembles, and focusing-defocusing dynamics of the PDF in our simulations are toy models of the micellar shape fluctuations. The second-moment tensor of the PDF is geometrically equivalent to a triaxial ellipsoid (with distinct semimajor axes but whose sum is fixed), and so the analogy is of micelles which are allowed to vary within isotropic conformations (spheres) and triaxial ellipsoids and of shear banding which correlates with the micelle fluctuations. Our model system of rigid-rod macromolecular dispersions is shown below to indeed generate shear bands which correlate with the focusing and defocusing and principal axis distortions of the PDF. As noted, we allow only spatial morphology in the velocity gradient direction spanning the plate gap. The study of two-dimensional (2D) spatial structure in the flow and orientation distribution has been carried out with second-moment closure models for the orientational distribution [53, 39, 27], which is a mesoscopic-macroscopic simulation, as well as a microscopic Smoluchowski integration coupled with the macroscopic Stokes equation [34, 60] or Navier–Stokes equation [26]. It is a topic of future interest to apply our 2D Smoluchowski–Navier–Stokes code to

Copyright © by SIAM. Unauthorized reproduction of this article is prohibited.

explore the stability of the results presented here to higher-dimensional perturbations.

Several recent review articles are suggested for further reading on this subject [8, 38, 40].

2. One-dimensional (1D) Smoluchowski–Navier–Stokes model. We consider nematic (rigid-rod) suspensions between two parallel plates which move at the same speed in opposite directions. Let $f(\mathbf{m}, \mathbf{x}, t)$ be the *orientational probability distribution function* for a given rod to have axis of symmetry $\mathbf{m}$ on the unit sphere. The Smoluchowski equation with flow field $\mathbf{v}$ is written in the internal time scale of the pure nematic liquid, $t = \tilde{t} D_r$, where $\tilde{t}$ is the laboratory time, and D_r is the average rotational diffusivity of the nematic liquid:

$$\begin{aligned} &\tfrac{Df}{Dt} = \mathcal{R} \cdot [(\mathcal{R} f + f \mathcal{R} V)] - \mathcal{R} \cdot [\mathbf{m} \times \dot{\mathbf{m}} f], \\ &\dot{\mathbf{m}} = \Omega \cdot \mathbf{m} + a[\mathbf{D} \cdot \mathbf{m} - \mathbf{D} : \mathbf{mmm}], \end{aligned} \tag{2.1}$$

where $D/Dt = \partial/\partial t + \mathbf{v} \cdot \nabla$, $\mathcal{R} = \mathbf{m} \times \frac{\partial}{\partial \mathbf{m}}$ is the rotational gradient operator, $\mathbf{D}$ and $\mathbf{\Omega}$ are the dimensionless rate-of-strain and vorticity tensors, respectively, and $a = \frac{r^2-1}{r^2+1}$, where r is the rod aspect ratio (the rod is a spheroid which has a well-defined aspect ratio). The Doi–Marrucci–Greco potential is

$$V = -\tfrac{3N}{2} \mathbf{M} : \mathbf{mm} - \tfrac{1}{2Er} [\Delta \mathbf{M} + \theta \, \nabla\nabla \cdot \mathbf{M}] : \mathbf{mm}, \tag{2.2}$$

where N is a dimensionless rod volume fraction which governs the strength of short-range excluded volume interactions, and $\theta > 0$ measures elastic anisotropy, which is positive for the rod-like dispersions considered here and corresponds in the Leslie–Ericksen limit to the rod ordering of elastic constants, with bend constant greater than the splay and twist constants. The Ericksen number $Er = \frac{8}{N} (\frac{h}{L})^2$ is the key distortional elasticity parameter, where $2h$ is the gap height, and L is the persistence length (or strength) of distortional elasticity. The rank 2 tensor $\mathbf{M}$ is the second moment of f,

$$\mathbf{M} = \mathbf{M}(f) = \int_{||\mathbf{m}||=1} \mathbf{mm} f(\mathbf{m}, \mathbf{x}, t) \, d\mathbf{m}. \tag{2.3}$$

The eigenvectors $\mathbf{n}_i$, $i = 1, 2, 3$, of $\mathbf{M}$ are the *nematic directors*, with corresponding ordered eigenvalues $0 \le d_3 \le d_2 \le d_1 \le 1$, $d_1 + d_2 + d_3 = 1$. The differences $s = d_1 - d_2$ and $\beta = d_2 - d_3$ are called the Flory and biaxiality *order parameters*, respectively, indicating relative degrees of orientation along the director axes. The peak axis of orientation, $\mathbf{n}_1$, is called the major director, whose dynamics is a standard measure of unsteady orientational distributions in shear flows.

We label x the flow direction, y the flow-gradient direction, and z the vorticity axis. In this paper, we neglect the variations in the flow direction and the vorticity direction. Only the structure along the flow-gradient direction is considered. The polar angle θ (measured from the vorticity axis) and azimuthal angle ϕ (measured from the positive x axis) of the major director $\mathbf{n}_1$ yield

$$\mathbf{n}_1 = (\sin\theta \cos\phi, \sin\theta \sin\phi, \cos\theta). \tag{2.4}$$

The nondimensional plate speed is determined by the Deborah number $De = \frac{v_0}{h \, D_r}$, which is the gap shear rate normalized by the molecular relaxation rate D_r, $\pm v_0$ are the physical plate speeds, and $2h$ is the gap width.

The dimensionless forms of the balance of linear momentum, the continuity equation, and the stress constitutive equation are

Copyright © by SIAM. Unauthorized reproduction of this article is prohibited.

$$
\begin{aligned}
\tfrac{d\mathbf{v}}{dt} &= \nabla\cdot(-p\mathbf{I}+\tau), \qquad \nabla\cdot\mathbf{v}=0,\\
\tau &= \mu_3(a)\mathbf{D}+\mu_1(a)(\mathbf{D}\cdot\mathbf{M}+\mathbf{M}\cdot\mathbf{D})+\mu_2(a)\mathbf{D}:\mathbf{M}_4\\
&+ a\alpha(\mathbf{M}-\tfrac{1}{3}\mathbf{I}-N\,\mathbf{M}\cdot\mathbf{M}+N\,\mathbf{M}:\mathbf{M}_4)\\
&- a\,\tfrac{\alpha}{6Er}(\Delta\mathbf{M}\cdot\mathbf{M}+\mathbf{M}\cdot\Delta\mathbf{M}-2\,\Delta\mathbf{M}:\mathbf{M}_4)\\
&- \tfrac{\alpha}{12Er}[2(\Delta\mathbf{M}\cdot\mathbf{M}-\mathbf{M}\cdot\Delta\mathbf{M})+\mathbf{M}_c]\\
&- a\,\tfrac{\alpha\theta}{12Er}[\mathbf{M}\cdot\mathbf{M}_d+\mathbf{M}_d\cdot\mathbf{M}-4(\nabla\nabla\cdot\mathbf{M}):\mathbf{M}_4]\\
&- \tfrac{\alpha\theta}{12Er}[\mathbf{M}_d\cdot\mathbf{M}-\mathbf{M}\cdot\mathbf{M}_d-\mathbf{M}_e],
\end{aligned}
\tag{2.5}
$$

where

$$\mathbf{M}_c=(\nabla\mathbf{M}:\nabla\mathbf{M}-(\nabla\nabla\mathbf{M}):\mathbf{M}), \tag{2.6}$$

$$\mathbf{M}_d=\nabla\nabla\cdot\mathbf{M}+(\nabla\nabla\cdot\mathbf{M})^T, \tag{2.7}$$

$$\mathbf{M}_e=(\nabla\nabla\cdot\mathbf{M})\cdot\mathbf{M}-\mathbf{M}_{\beta j,\alpha}\mathbf{M}_{ij,i}, \tag{2.8}$$

$$\mathbf{M}_4=\int_{||\mathbf{m}||=1}\mathbf{mmmm}\,f(\mathbf{m},\mathbf{x},t)\,d\mathbf{m}. \tag{2.9}$$

$\mu_3(a)$ is the shape dependent viscosity parameter (whose reciprocal is the effective Reynolds number of the dispersion with solvent and dispersion contributions), μ_1 and μ_2 are two other flow-nematic dimensionless viscosity parameters, and $\alpha = 3\nu kT/\tau_0$ (ν is the number density of nematic molecules, k the Boltzmann constant, and T the absolute temperature) measures the relative strength of entropic fluctuations of the rod macromolecules.

We choose a very high rod aspect ratio so that $a \approx 1$. From [20, 24], we choose excluded volume and flow parameters that resonate monodomain rheochaos (for imposed simple shear): $N = 5.2$ ($\sim 1\%$ volume fraction of nematogens of diameter 2 nm and length 200 nm) and $De = 4.04$ (the chaotic range is $2.69 < De < 4.10$). In the coupled flow-nematic system, the distortional elasticity determines the steady versus dynamic response as well as the plate anchoring conditions. For sufficiently low Er, the liquid stores all stresses generated by plate motion in a steady state structure [19, 7]. At some critical Er, a transition to dynamic structure evolution arises [57, 42, 25]. We present results for $Er = 500$, chosen to illustrate long-time behavior which retains rheochaos across the gap in the presence of spatial morphology that can be resolved with our present algorithm [64]. Parameter sweeps are numerically prohibitive, especially at higher Er, for multiple reasons: length scales of morphology diminish with some inverse power of the Ericksen number [43, 53, 19, 7], including sharp boundary layers near defects which are not a priori known; this leads to a very small CFL condition for numerical stability, and yet one still must simulate for long times to get trustworthy time series. We further choose $\mu_3 = 0.1$, $\mu_1 = 0.0004$, $\mu_2 = 0.15$, $\alpha = 2$, $\theta = 0.5$, corresponding to nominal values of a rod-like nematic polymer dispersion. The simulations reported here are restricted to this one parameter set, with longtime numerical integration and spatial resolution, followed by postprocessing of the data for imaging, time series analysis, and spatial decomposition.

Remarks on boundary anchoring conditions. At the plates, we posit that the nematic liquid achieves an equilibrium set by the excluded volume potential; this im-

Copyright © by SIAM. Unauthorized reproduction of this article is prohibited.

plies that rest states prior to flow are homogeneous. Wall conditions could be modified dramatically due to chemical interactions with the plates, which would then establish a morphology in rest states that depends on how different the plate conditions are with respect to one another and the interior rest equilibria. Mismatch boundary conditions have been explored [62] with second-moment models, but not here, since we want to isolate the spatial features due only to interior chaotic dynamics and a pure equilibrium anchoring condition. Thus, prior to onset of the plates, the nematic liquid is assumed to be in a uniform, uniaxial nematic equilibrium. The equilibrium order parameters are $s = 0.75$, $\beta = 0$ for a normalized concentration $N = 5.2$. Recall that nematic equilibria are rotationally invariant, in that the peak orientation of the PDF is arbitrary. The wall anchoring condition on the PDF selects this peak direction, which then breaks the degeneracy across the entire gap, and so the initial data is uniquely specified. In these simulations, we fix a "tilted" anchoring condition on $\mathbf{n}_1$: $\theta = \phi = 60^\circ$, which is chosen to stimulate out-of-plane behavior. We note that in-plane anchoring conditions ($\theta = \frac{\pi}{2}$) will suppress out-of-plane behavior and can lead to arrest of chaotic behavior in layers buffering the plates. The penetration depth of the plate layers is sensitive to anchoring conditions as well as the subsequent flow feedback behavior in the velocity field. These sensitivities are important and worth further study but also will not be explored here. All of these sensitivities are compounded by the application of second-moment closure models, which is the primary motivation for our investment in a resolved Smoluchowski equation solver with full coupling to the Navier–Stokes flow equation.

Remarks on the numerical method and model parameters. Our numerical method is detailed in [64]. To summarize, we expand the PDF in spherical harmonics up to order $L = 10$ (equivalently, 65 real degrees of freedom), with y and t dependent amplitudes, which converts the Smoluchowski equation into a system of PDEs for the amplitude functions, which are of nonlinear reaction-diffusion type. The spatial derivatives are then discretized using standard fourth-order finite differences, and a large system of temporal ODEs is produced from the method of lines. Finally, we numerically integrate the ODE system with a spectral deferred correction algorithm [11, 31] that provides fourth-order accuracy.

3. Monodomain rheochaos in the longwave, flow-imposed limit.

To lay a baseline for the heterogeneous simulations, we recall statistical properties associated with monodomain rheochaos [30, 20]. This simulation is the longwave limit, corresponding to a reduction imposed by a homogeneous PDF, no flow feedback (simple linear flow and a homogeneous PDF yield automatic solution of the Navier–Stokes flow equation), and no influence of the plate anchoring conditions (the PDF is uniform in space). A simple shear flow is imposed, $v_x(y) \equiv 4.04y$, with Deborah number $De = 4.04$ which lies within the chaotic window documented in [20]. The data from the first 20,000 time units are discarded so that data reported are safely on the apparent chaotic attractor.

Figure 1 shows the orbit of the major director $\mathbf{n}_1(\mathbf{M}(f))$, the peak axis of the PDF, in the next 10,000 time units. These results are postprocessed from the full resolved simulations, which involves projection of the PDF onto the first five complex spherical harmonics, which determines the second-moment tensor $\mathbf{M}$ of the PDF, and then computation of the eigenvalues and eigenvectors of the rank 2, second-moment tensor. The director orbit shown in Figure 1 clearly jumps between the Larson–Ottinger kayaking state ($\mathbf{K}_1$, where the director rotates about the vorticity axis) and the pair of tilted kayaking states ($\mathbf{K}_2^{\pm}$, where the director rotates about an axis tilted

Copyright © by SIAM. Unauthorized reproduction of this article is prohibited.

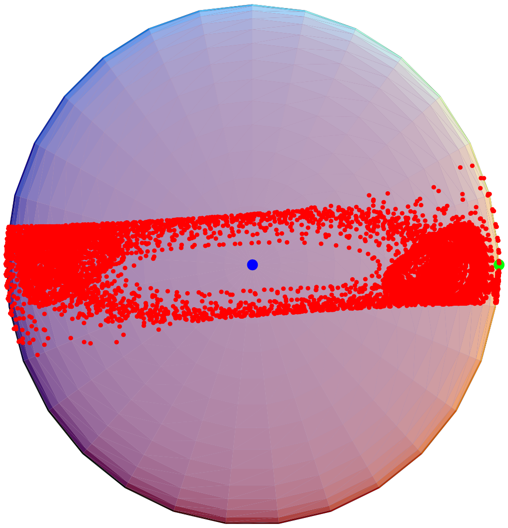

Fig. 1. *The orbit of the major director (peak axis of the PDF) for a chaotic monodomain attractor at* $De = 4.04$, *with imposed simple shear* $v_x(y) \equiv 4.04y$. *The black dot at the center indicates the vorticity axis.*

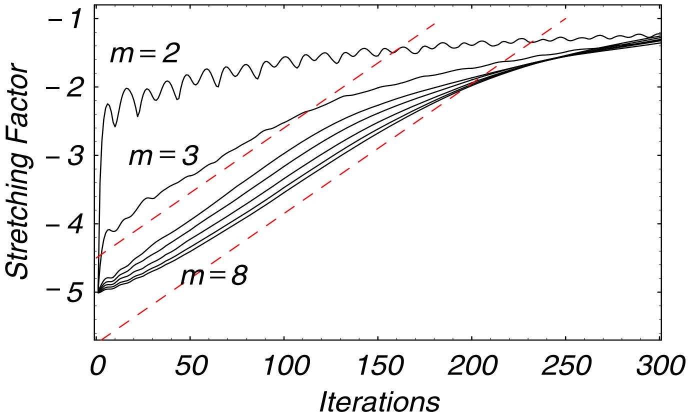

Fig. 2. *Monodomain rheochaos. Stretching factor versus iterations (based on the software TISEAN* [32]*). The solid lines show the stretching factor using several embedding dimensions:* $m = 2, 3, 4, 5, 6, 7, 8$. *The dashed lines show the least squares fit of the tangent line for* $m > 3$, *whose slope* (≈ 0.016) *is the leading Lyapunov exponent.*

between the vorticity axis and the shear plane). This orbit presents a Bernoulli shift on three symbols, the symmetric kayaking orbit and the twin pair of reflection-symmetric tilted kayaking orbits.

In Figure 2 we compute the stretching factor versus the embedding dimension and the leading Lyapunov exponent (the slope of the stretching factor) of the PDF time series to quantify the apparent chaos depicted in the director orbit. To make contact with Grosso et al. [30], we use the same software TISEAN [32]. It is clearly seen that, before the saturation at about 200 iterations and for embedding dimension

Copyright © by SIAM. Unauthorized reproduction of this article is prohibited.

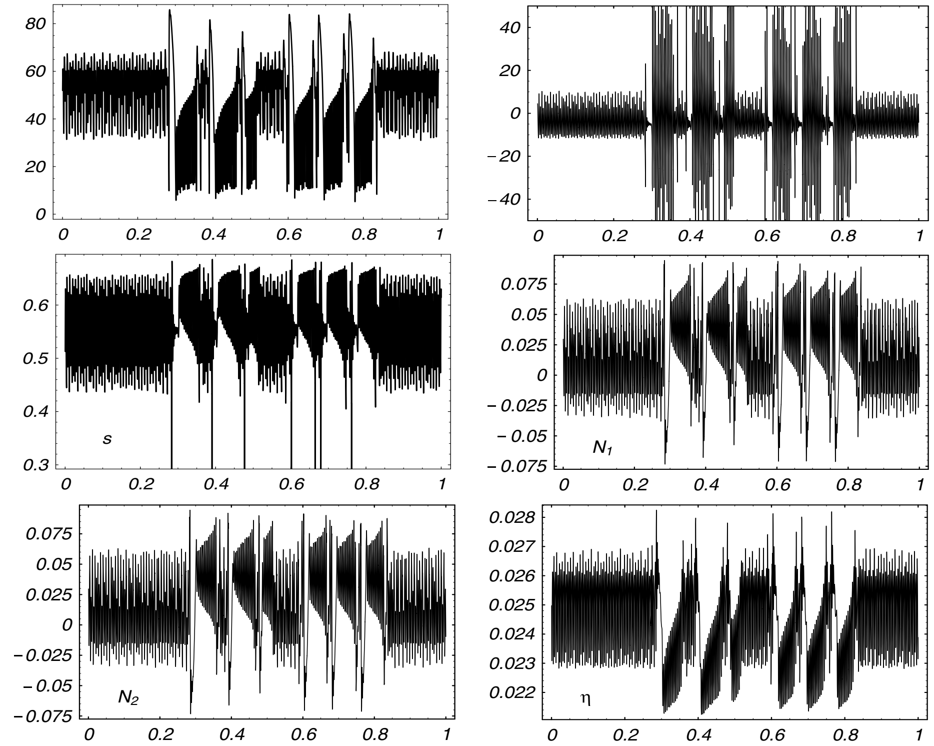

Fig. 3. *Monodomain rheochaos. Times series of the aximuthal angle ϕ (top left) and polar angle θ (top right) of the major director (peak axis of the PDF), Flory order parameter s (middle left), first normal stress difference N_1 (middle right), second normal stress difference N_2 (bottom left), and normalized shear stress τ_{xy} (bottom right) for* 1100 *nondimensional time units. (The horizontal axis has been normalized by the entire time interval.)*

$m \geq 4$, the stretching factor is almost linear. The least squares fit gives a positive slope about 0.016, which determines the leading Lyapunov exponent, whose positivity confirms the chaotic behavior of the orbit.

Figure 3 shows the apparently chaotic time series of other quantities, including the alignment angle θ (polar) and ϕ (azimuthal), birefringence order parameter $s = d_1 - d_2$ (where d_1 and d_2 are the two largest eigenvalues of the second-moment tensor $\mathbf{M}$), normal stress differences $N_1 = \tau_{xx} - \tau_{yy}$ and $N_2 = \tau_{yy} - \tau_{zz}$, and the shear stress τ_{xy}. The middle part of the time interval $(0.3, 0.85)$ exhibits orbits similar to the $\mathbf{K}_1$ kayaking state, while other segments of the orbit shadow the $\mathbf{K}_2$ tilted kayaking state.

This solution of the Smoluchowski equation, representative of homogeneous monodomain rheochaos, is now injected into a heterogeneous simulation by retaining the same volume fraction N (strength of the excluded volume potential) and the same bulk plate-imposed Deborah number De by controlled velocities of top and bottom plates. However, now we impose an anchoring condition on the PDF at each plate together with no-slip on velocity. This leads to spatial conflict between the mid-gap propensity toward bulk rheochaos shown here and steady PDF anchoring at the plates. This PDF gradient morphology then creates stress gradients which couple back to flow, whose outcome we turn to now.

Copyright © by SIAM. Unauthorized reproduction of this article is prohibited.

4. Persistence of rheochaos with heterogeneity and flow coupling. We turn now to the flow-PDF structure simulation which releases the longwave limit imposed in the above monodomain simulation. We use 401 uniform grid points across the plate gap, which are chosen to safely resolve all spatial structures. A fixed time step $2 \cdot 10^{-3}$ is used in the integration scheme, which corresponds to 500 time steps per unit of molecular relaxation. The data is recorded every 0.1 time unit (50 time steps). We discard the first 2500 time units (over 10^6 time steps) to allow saturation onto the attractor and then store the next 1500 time steps for the postprocessing data analysis and figures to follow.

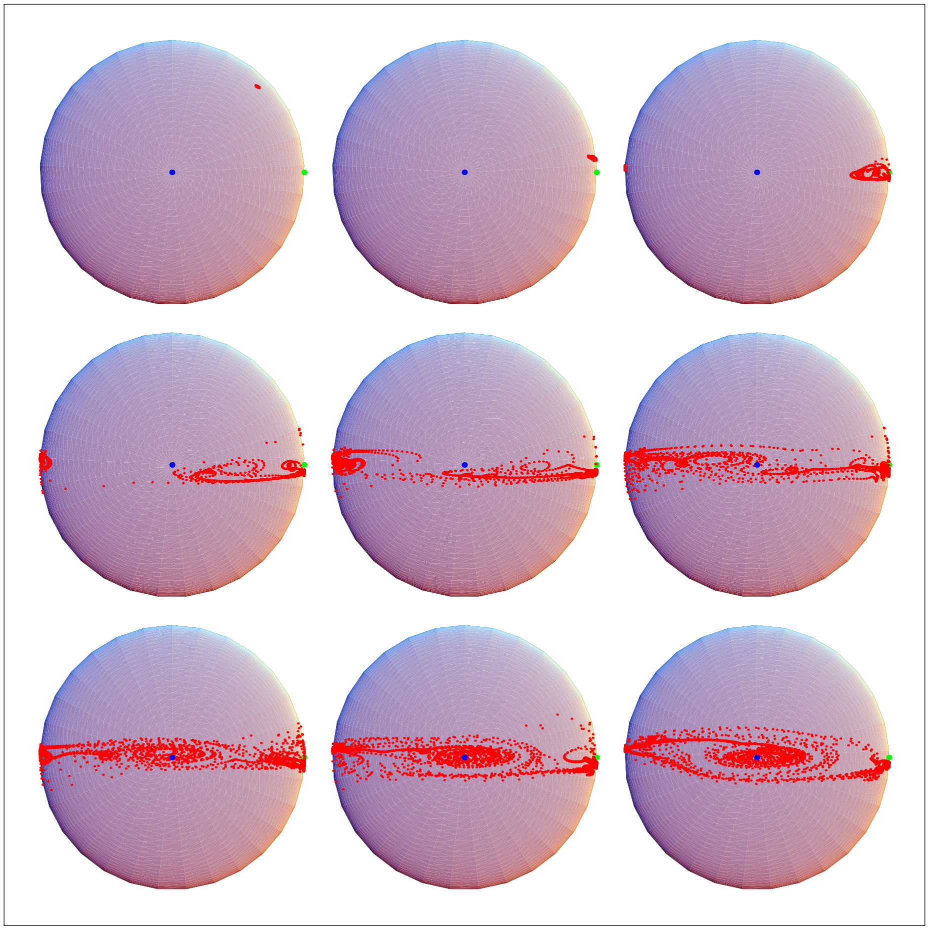

FIG. 4. *Heterogeneous rheochaos. Major director orbits on the unit sphere at several physical locations from nearby the top plate to the midgap:* $y = 0.98, 0.86, 0.74, 0.62, 0.5, 0.38, 0.26, 0.14, 0.0$. *The dot in the center shows the vorticity axis; the dot on the right shows the flow axis. The clock time in molecular relaxation units is from* 2500 *to* 3000, *long after transients have passed.*

4.1. Dynamical signatures of rheochaos at fixed heights in the shear gap. Figure 4 depicts the orbit of the major director at nine different gap locations ($y = 0.0$ indicates the gap center, while $y = 1.0$ is the top plate). At interior locations $y = 0.0, 0.14, 0.26$, one finds chaotic orbits typical of sheared monodomains [52, 18, 30, 20, 51] as shown in Figure 1. The major director exhibits a random jump between a kayaking limit cycle ($\mathbf{K}_1$) (where $\mathbf{n}_1$ oscillates around the vorticity axis) and a

Copyright © by SIAM. Unauthorized reproduction of this article is prohibited.

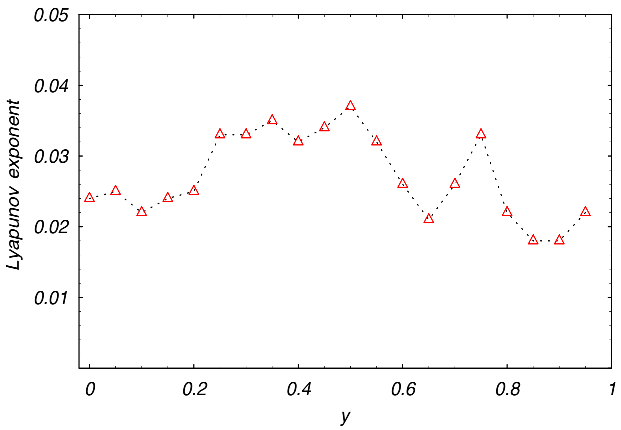

Fig. 5. *Heterogeneous rheochaos. Lyapunov exponents across the shear gap produced from one spherical harmonic amplitude of the PDF.* $y = 0$ *indicates the gap center, while* $y = 1$ *indicates the top plate position.*

symmetric pair of tilted kayaking orbits ($\mathbf{K}_2^{\pm}$) (where $\mathbf{n}_1$ oscillates around an axis tilted between the vorticity axis and shearing (x-y) plane). At $y = 0.62$, closer to the top plate, the orbit traced by the peak of the PDF jumps between "tilted kayaking" limit cycles that surround a direction that lies between the vorticity axis and shear plane. Closer to the plates, at $y = 0.74, 0.86$, the orbits cover a small region surrounding one tilted kayaking limit cycle, with axis of symmetry close to the flow direction. There is a thin boundary layer in which the PDF sharply transitions (compare orbits at $y = 0.86$ and $y = 0.98$) to the plate anchoring condition.

Next, we compute the leading Lyapunov exponent of the PDF time series at different gap heights to quantify the apparent chaos depicted in the major director. The result is shown in Figure 5. The leading exponent is positive everywhere across the interior of the gap, which confirms chaotic behavior in the entire interior of the gap. Remarkably, rather than reduce the exponent as one might intuitively expect, the coupling with hydrodynamics yields greater Lyapunov exponents at each interior grid point than the monodomain limit.

Figure 6 shows apparently chaotic time series of the polar angle θ, the azimuthal angle ϕ of the major director, and the birefringence order parameter s at six different gap heights: $y = 0.98, 0.78, 0.58, 0.38, 0.18, 0.0$. Near the plate ($y \approx 1$), the amplitude of the oscillation is relatively small. Yet, at all gap heights shown, all quantities show erratic fluctuations. Further evidence appears in Figure 7, showing time series of the first normal stress difference $N_1 = \tau_{xx} - \tau_{yy}$ (left), second normal stress difference $N_2 = \tau_{yy} - \tau_{zz}$ (middle), and shear stress τ_{xy} (right) at the same gap heights. These erratic stress fluctuations are the basis for the term "rheological chaos."

We thus confirm results in [6] on the persistence of chaotic time series coupled with structure in confined plate gap simulations. Our simulations generalize [6] in two significant directions: from a second-moment orientation tensor (five components) to 65 component resolution of the PDF; and from imposed simple shear flow to full hydrodynamic coupling. These Navier–Stokes and Smoluchowski coupled simulations, followed by postprocessing of the dynamical data, show that (i) orientational chaos persists in the presence of PDF gradients and with hydrodynamic coupling; and (ii) the velocity field also exhibits irregular fluctuations in the interior of the cell.

Copyright © by SIAM. Unauthorized reproduction of this article is prohibited.

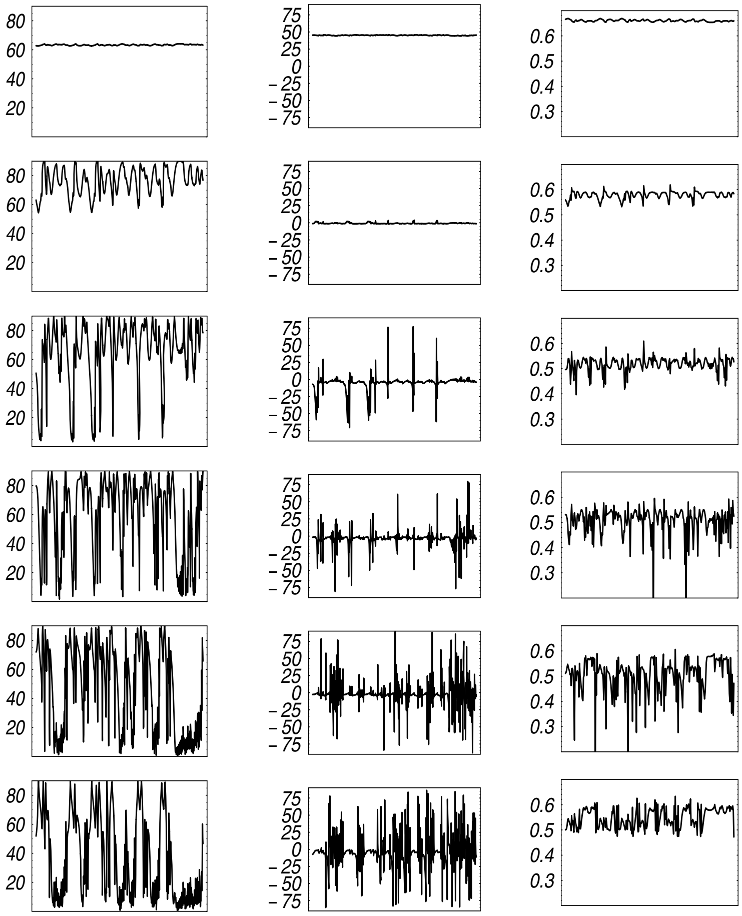

FIG. 6. *Heterogeneous rheochaos. Time series of the polar angle (left column), the azimuthal angle (middle column), and the order parameter s (right column) computed from the PDF at six different gap locations. From top to bottom:* $y = 0.98, 0.78, 0.58, 0.38, 0.18, 0.0$. *The horizontal axis covers the time interval* $[2500, 4000]$.

4.2. Space-time surface and level contours of PDF, stress, and flow.

We now present the time evolution of gap structures through surface and contour plots of the PDF, stress, and flow field. In this subsection, we focus on the combined space-time pictures, beginning with features of the PDF.

Recall that the Flory order parameter s is a scalar feature of the orientational distribution which conveys “shape deformations” of the PDF through the difference between the leading two principal eigenvalues of the second-moment tensor. Large values of s correspond to focusing of the rod ensemble along the major director, whereas values approaching $s = 0$ reflect a defocusing of the ensemble. The extreme value $s = 0$ corresponds to a degenerate phase, called a defect, where the principal axis of orientation is a linear space of dimension at least 2. These *isotropic defect structures* have no analogue in the Leslie–Ericksen–Frank (LEF) theory typically applied to small molecule liquid crystals. We note for the nonexpert that in nematic polymers where the rods are significantly larger than in liquid crystals, the phenomenon of defects is richer. LEF models posit a unique director and assume $s \sim 1$ so that the PDF is a

Copyright © by SIAM. Unauthorized reproduction of this article is prohibited.

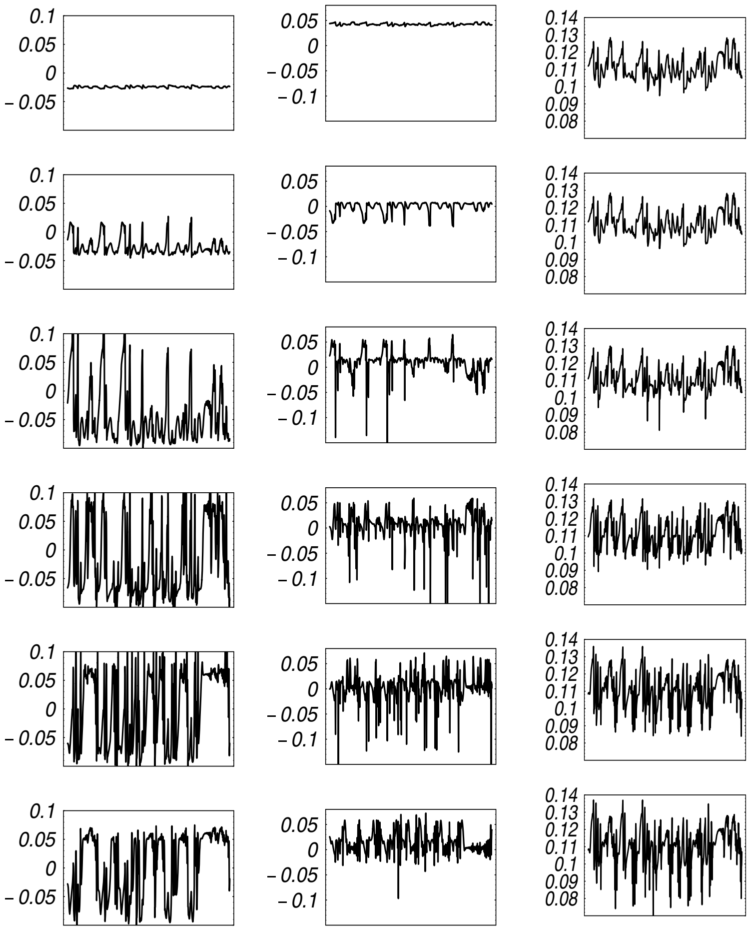

Fig. 7. *Heterogeneous rheochaos. Time series (from* $t = 2500$ *to* 4000*) of normal stress differences* N_1 *(left column),* N_2 *(middle column), and shear stress* τ_{xy} *(right column) at six different locations. From top to bottom:* $y = 0.98, 0.78, 0.58, 0.38, 0.18, 0.0$.

Dirac distribution localized around the distinguished director. In LEF theory, defects are necessarily "nematic" in nature, associated with the winding number (geometric invariants) of the director field. A key distinction is that LEF defects are permanent and cannot "escape" dynamically through order parameter degrees of freedom in the PDF. These director defects of LEF theory are captured by the Doi–Hess PDF theory, corresponding to director-dominated distortions where the order parameter s remains bounded far away from 0. These director defects are not detectable in one dimension, since one cannot discuss a closed space curve or surface. However, disordered isotropic defect structures are possible even in homogeneous monodomains. We have shown in monodomain simulations that transient isotropic defect events indeed occur in chaotic attractors [20]; that is, they are local time events. We refer the reader to Sonnet, Killian, and Hess [54] for an amplified discussion of the alignment tensor versus director description. We monitor the persistence of isotropic defect events in the next figures, with the observation that they are local in time and space.

Figure 8 shows the space-time structures of the Flory order parameter s in the time interval $[2500, 4000]$ (top row) and a blowup of the interval $[2700, 2800]$ (bottom

Copyright © by SIAM. Unauthorized reproduction of this article is prohibited.

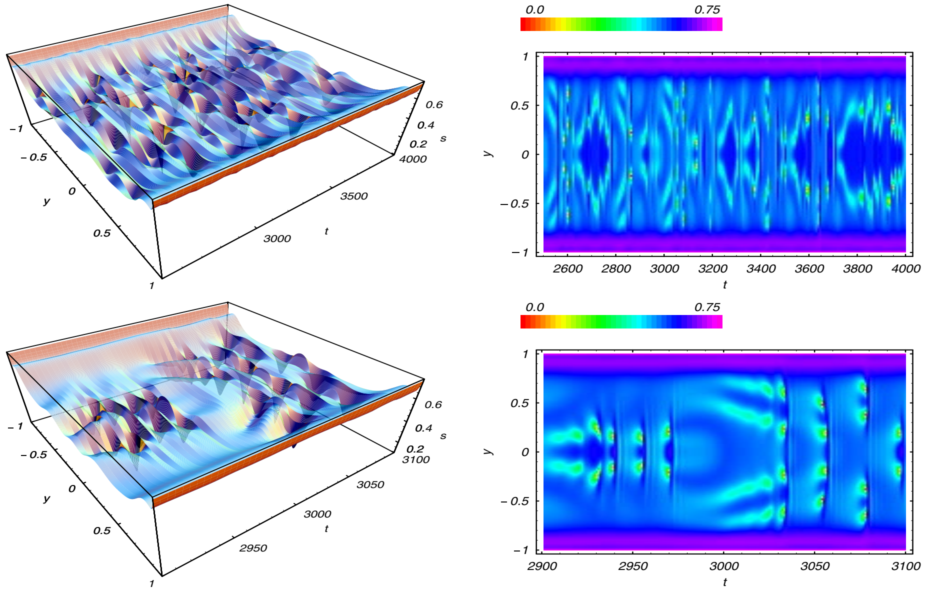

FIG. 8. *Heterogeneous rheochaos. The surface plot (left) and contour plot (right) of the order parameter* $s = d_1 - d_2$ *over times* $[2500, 4000]$ *in the top row and times* $[2700, 2800]$ *in the bottom row to amplify defect events.*

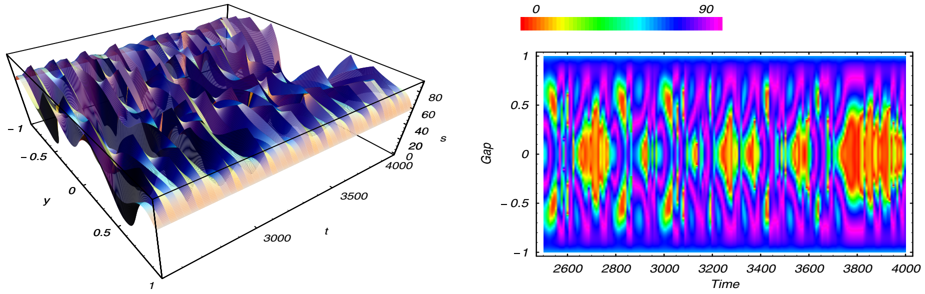

FIG. 9. *Heterogeneous rheochaos. The surface plot (left) and contour plot (right) of the polar angle* $\theta(y, t)$ *of the major director.*

row); surfaces are given on the left and their projection onto level set contours on the right. The blowup highlights intermittent isotropic defect events, local in space and time, in which the order parameter s spikes toward 0. These defect cores (one on each side of the gap) spawn, intensify, propagate, weaken, and then "melt" during this 100 time unit span; clearly they are not permanent structures, quite distinct from winding number "nematic defects" which exist only in higher space dimensions.

The spatio-temporal structure of the polar angle (θ) of the major director $\mathbf{n}_1$ is shown in Figure 9, where 0° corresponds to vorticity alignment and 90° corresponds to in-plane orientation. The polar angle reflects transitions of the PDF peak direction in and out of the shear plane, which are remarkably correlated with the isotropic defect events by comparison with Figure 8. The erratic dynamic fluctuations in s and θ, observed in time series earlier, are evident in these figures if one fixes attention to one gap height; yet in any snapshot, there is relative smoothness in the order parameter and polar angle spatial variations. We return to these spatial snapshot

Copyright © by SIAM. Unauthorized reproduction of this article is prohibited.

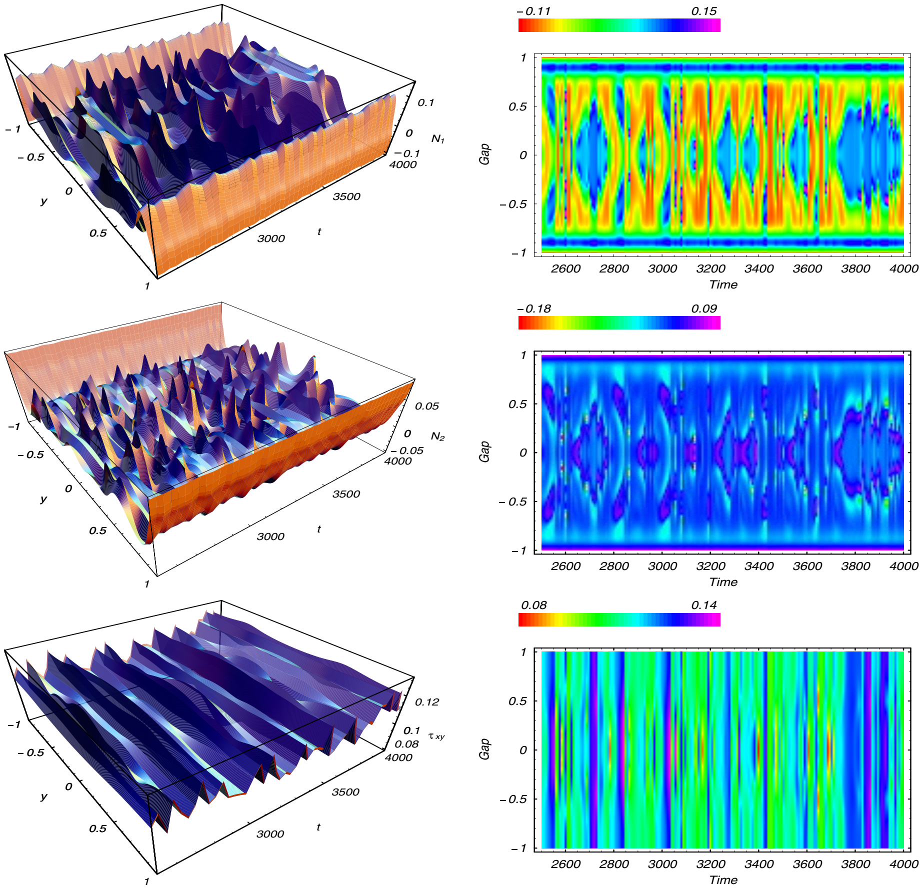

Fig. 10. *Heterogeneous rheochaos. Surface plot (left) and level contour plot (right) of the normal stress differences* $N_1(y,t)$ *(top),* $N_2(y,t)$ *(middle), and shear stress* $\tau_{xy}(y,t)$ *(bottom).*

features shortly. The rheological stress features of $N_1(y,t)$, $N_2(y,t)$, and $\tau_{xy}(y,t)$ are shown in Figure 10. The first and second normal stress differences also show complex dynamics and spatial gradient structure, which are also correlated with the isotropic defect events and in-plane/out-of-plane director transitions. (Note the absolute values of N_2 range below .05 so that the surface plot exaggerates the gradients.) The shear stress is relatively tame, exhibiting intriguing shear thinning and thickening events which are nearly spatially uniform.

Figure 11 shows surface plots of the primary velocity v_x and the local Deborah number (normalized velocity gradient)

$$De^{loc} = \frac{\partial v_x}{\partial y}. \tag{4.1}$$

The primary velocity is a weakly nonlinear shear structure across the gap, with mild dynamic fluctuations of the full gap profile. There is clear evidence of shear banding but nowhere near the strong shear bands observed in mesoscopic second-moment tensor models (cf. [42, 63]). The most vivid non-Newtonian flow feedback is captured by the local Deborah number. We recall from [21, 23] that an imposed

Copyright © by SIAM. Unauthorized reproduction of this article is prohibited.

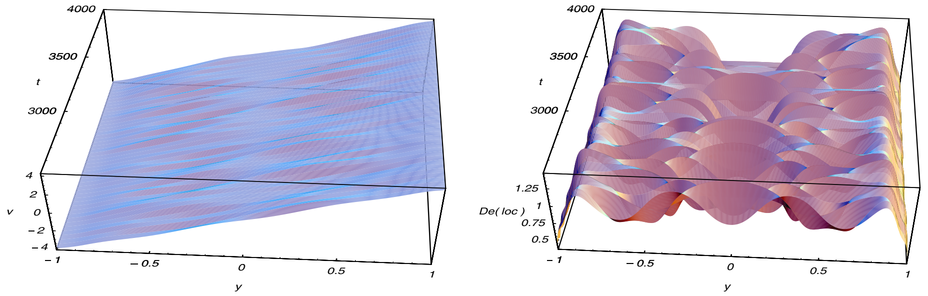

FIG. 11. *Heterogeneous rheochaos. Surface plots of the velocity field and local Deborah number (normalized velocity gradient).*

fixed Deborah number, if $\partial f/\partial y = 0$ and if $\partial^2 v_x/\partial y^2 = 0$, will produce a spectrum of unique, bistable, and tristable monodomain responses, including chaotic attractors for $2.69 \leq De \leq 4.10$, traditional kayaking ($\mathbf{K}_1$) orbits for $0 \leq De \leq 3.99$, and tilted pairs of kayaking ($\mathbf{K}_2^{\pm}$) orbits for $2.53 \leq De \leq 2.69$ and $4.10 \leq De \leq 4.65$. In this heterogeneous simulation, the local Deborah number, Figure 11 (right), fluctuates significantly at each gap height, and varies across the gap in each snapshot, so that selection mechanisms for local monodomain phases involve previous history and spatial correlations. The role of spatial gradients in biasing the likelihood statistics when there are multiple monodomain attractors [61] has not been explored in any systematic way.

4.3. Flow time series. Figure 12 further shows irregular velocity (left) and local Deborah number (right) time series at each fixed gap height (same heights as in Figure 6 and Figure 7), except the symmetry-constrained zero velocity at the midgap. These results show significant flow feedback, and thereby strong momentum and energy transfer between the solvent and rod ensemble. This flow feedback behavior suggests caution should be taken in application of models with an imposed simple shear flow in the presence of chaotic orientational dynamics. Note the local Deborah number exhibits strong amplitude fluctuations even close to the plates.

Near each plate, for $|y|$ between 0.9 and 1, there is a robust gradient layer with small dynamic fluctuations, even though De^{loc} is inside the chaotic range for sheared monodomains (fluctuating between 1.9 and 2.6; see Figure 12, top right). This behavior suggests the extended influence of confined wall anchoring to penetrate well into the shear gap and arrest dynamic tumbling and kayaking dynamics, confirmed by the $y = 0.98$ (near wall) director time series of Figure 4. Proceeding further into the shear gap, for $|y|$ around 0.78, De^{loc} fluctuates in space and time between 4.25 and 5.75 (Figure 12, row 2, right column). These values often lie outside the monodomain chaotic De range, and so irregular dynamic fluctuations in De^{loc} appear to be responsible for the chaotic PDF time series at $y = 0.74$ (Figure 4). Next, in the large interior gap layer for $|y|$ between 0 and 0.7, snapshots of De^{loc} reflect significant temporal fluctuations among laminar spatial profiles, with local values ranging mostly within the chaotic monodomain range. This is indicative of a strong chaotic dynamics of the interior shear layer but with spatial coherence at each fixed time.

These spatio-temporal features of De^{loc} are remarkably correlated with those of the PDF (Figure 4) and stored stresses (Figure 10). The highlights are boundary wall layers that exhibit robust spatial profiles which fluctuate very little; a large interior gap layer with strong temporal fluctuations between qualitatively different

Copyright © by SIAM. Unauthorized reproduction of this article is prohibited.

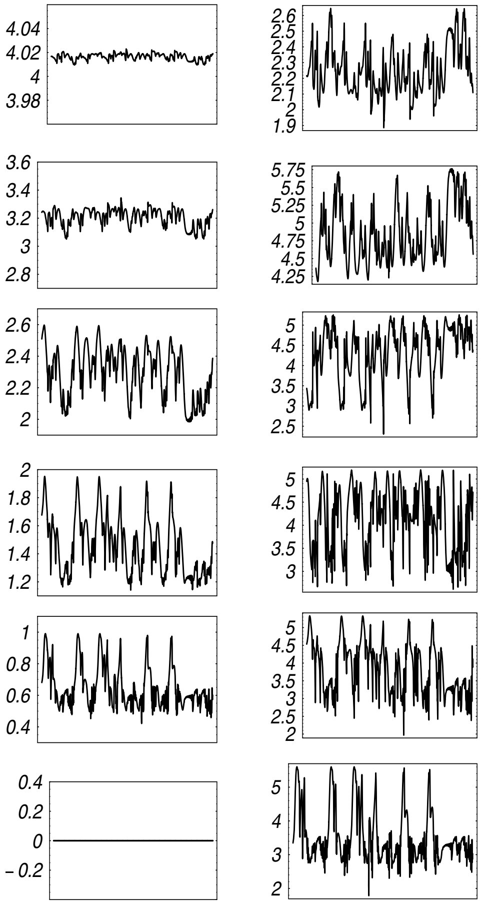

FIG. 12. *Heterogeneous rheochaos. Time series (from* 2500 *to* 4000*) of the velocity* v_x *(left column) and the local Deborah number* dv_x/dy *(right column) at* 6 *different gap locations. From top to bottom:* $y = 0.98, 0.78, 0.58, 0.38, 0.18, 0.0$.

spatial structures; and a transition layer between $|y| = 0.7$ and 0.9 with intermediate dynamic fluctuations among similar laminar structures.

We turn now to a detailed amplification of the spatial features across the plate gap to complement the dynamical signatures of temporal chaos.

4.4. Heterogeneous rheochaos: Evidence for spatial coherence. Figure 13 gives four snapshots of the structure in the half-gap $0 \leq y \leq 1$ of the velocity v_x, local Deborah number De^{loc}, order parameter s, polar angle of the major director θ, first normal stress difference N_1, and the shear stress τ_{xy}. Each scalar structure varies significantly across the four snapshots, yet each spatial profile is relatively smooth, providing evidence for spatial coherence.

Figure 14 presents time averages of all properties shown in Figure 13 over the time interval $[2500, 4000]$, which gives some intuition for the mean spatial structure in the PDF, flow, and stress. The mean velocity structure has a localized boundary layer at each plate and then a slightly modulated linear profile across the gap. The modulations of v_x are described by the mean local Deborah number (velocity gradi-

Copyright © by SIAM. Unauthorized reproduction of this article is prohibited.

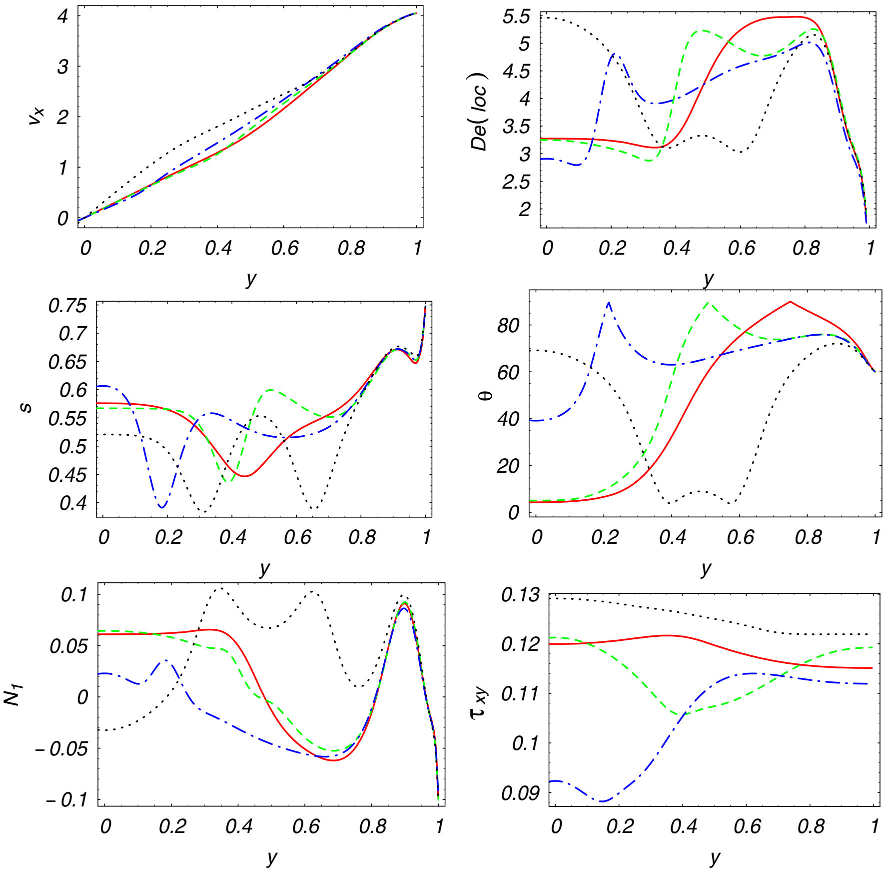

FIG. 13. *Heterogeneous rheochaos: Snapshots of the primary velocity profile* $v_x(y, t_k)$ *(top left),* $De^{loc}(y, t_k)$ *(top right),* $s(y, t_k)$ *(middle left),* $\theta(y, t_k)$ *(middle right),* $N_1(y, t_k)$ *(bottom left), and* $\tau_{xy}(y, t_k)$ *(bottom right) across the half plate gap* $(0 \leq y \leq 1)$ *at four snapshots:* $t_k = 2680$ *(solid line),* 2730 *(dashed line),* 2780 *(dot-dashed line),* 2830 *(dotted line).*

ent), which shows the plate layer where the flow accelerates, and then decelerates in the midgap, with the overall average De matching the plate-imposed mean value 4.04. The order parameter structure shows that on average the PDF defocuses away from the plates, with spatial variations on shorter length scales than the flow and director structures. The first normal stress difference is negative at the plates, nearly zero in the midgap, and then exhibits an overshoot-undershoot phenomenon in between. The shear stress varies least among all flow-PDF features, with strongest average shear stress at the midgap.

5. Concluding remarks. We have presented results of a coupled microscopic (Doi–Hess kinetic theory) and macroscopic (1D Navier–Stokes) simulation of rigid-rod macromolecular dispersions, at parameter values where the longwave dynamics is chaotic. The main goal is to ascertain how monodomain rheochaos saturates in the presence of both heterogeneity (gradient elasticity) of the PDF and hydrodynamic feedback. All statistical features (time series, Lyapunov exponents, graphical orbits) indicate classical signatures of chaotic intermittency at each interior gap height so that chaotic dynamics persists in the flow-PDF space-time system. Indeed, the velocity time series appears to inherit the chaotic behavior, and the leading Lyapunov

Copyright © by SIAM. Unauthorized reproduction of this article is prohibited.

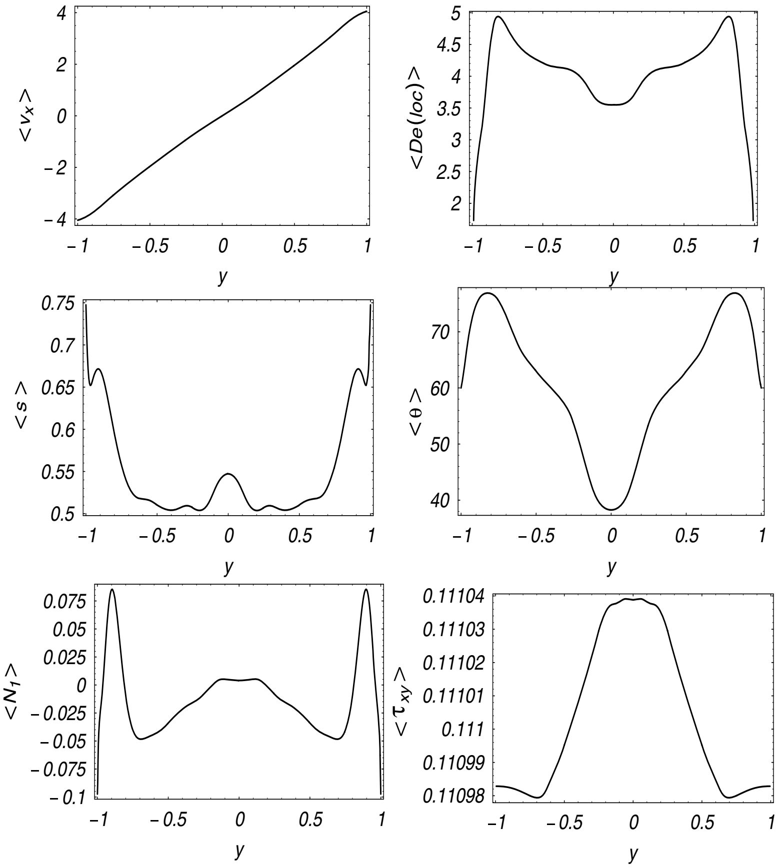

Fig. 14. *Heterogeneous rheochaos. Averages of primary velocity* v *(top left), local Deborah number* $\partial v_x/\partial y$ *(top right), Flory order parameter* s *(middle left), polar angle of the peak PDF axis* θ *(middle right), first normal stress difference* N_1 *(bottom left), and shear stress* τ_{xy} *(bottom right) in the time interval* $[2500, 4000]$.

exponents across the gap of the coupled flow-PDF system are greater than the monodomain leading Lyapunov exponent. If anything, flow coupling and distortional elasticity have enhanced the traditional signatures of rheochaos!

The next important question addressed relates to the spatial structures which form across the gap in the presence of chaotic dynamics. Recall that the PDF structures are necessarily generated due to plate anchoring of the PDF which is in conflict with interior dynamic fluctuations, and then these PDF gradients induce stress gradients which provide feedback to generate nonlinear flow perturbations to the plate-imposed simple shear profile. We find coherent spatial profiles in both the PDF and the flow at each snapshot, with no evidence for spatial chaos at these parameter values. Overall, these numerical results of the full kinetic-flow equations predict that nematic polymer suspensions driven by steady planar shear cells will exhibit persistent orientational and rheological chaos in a large interior cell layer, even with the inclusion of spatial heterogeneity and non-Newtonian hydrodynamic feedback. This prediction is consistent with the experimental observations of Berry and collaborators and with Berry's private communications [55].

These results are furthermore consistent with the 2D second-moment orientation

Copyright © by SIAM. Unauthorized reproduction of this article is prohibited.

tensor plus flow simulations of [27] but do not confirm the mesoscopic tensor 1D results with imposed flow reported by [6]. Whether this discrepancy is due to failure to allow flow coupling, due to a completely different Ericksen number regime, or due to an extremely large plate gap is not known, and the details are not discernible from this short letter [6].

The persistence of these chaotic statistical features with laminar spatial morphology in higher-dimensional spatial simulations remains for future study with the aid of our recently documented 2D Navier–Stokes–Smoluchowski algorithm [26]. We note that reduced-order modeling with the aid of second-moment Landau–de Gennes models has thus far reproduced all specific attractors determined from highly resolved kinetic simulations. We anticipate that the same low-order modeling of spatio-temporal attractors is possible, with the proviso that the parameters in the reduced-order model have to be adjusted to match the resolved system. This identification between attractors of the flow-nematic kinetic and moment-closure systems will play a vital role in numerical exploration of the large parameter space.

REFERENCES

[1] R. Bandyopadhyay, G. Basappa, and A. K. Sood, *Linear and nonlinear rheology of wormlike micelles*, Pramana, 53 (1999), pp. 223–235.

[2] R. Bandyopadhyay, G. Basappa, and A. K. Sood, *Observation of chaotic dynamics in dilute sheared aqueous solutions of CTAT*, Phys. Rev. Lett., 84 (2000), pp. 2022–2025.

[3] R. Bandyopadhyay and A. K. Sood, *Chaotic dynamics in shear-thickening surfactant solutions*, Europhys. Lett., 56 (2001), pp. 447–453.

[4] P. T. Callaghan, *Rheo-NMR: Nuclear magnetic resonance and the rheology of complex fluids*, Rep. Prog. Phys., 62 (1999), pp. 599–670.

[5] P. T. Callaghan, M. E. Cates, C. J. Rofe, and J. B. A. F. Smeulders, *A study of the spurt effect in wormlike micelles using nuclear magnetic resonance microscopy*, J. Phys. II, 6 (1996), pp. 375–393.

[6] B. Chakrabarti, M. Das, C. Dasgupta, S. Ramaswamy, and A. K. Sood, *Spatio-temporal rheochaos in nematic hydrodynamics*, Phys. Rev. Lett., 92 (2004), 188301.

[7] Z. Cui, M. G. Forest, Q. Wang, and H. Zhou, *On weak plane Couette and Poiseuille flows of rigid rod and platelet ensembles*, SIAM J. Appl. Math., 66 (2006), pp. 1227–1260.

[8] M. M. Denn and A. D. Rey, *Dynamical phenomena in liquid-crystalline materials*, in Annual Review of Fluid Mechanics 34, 2002, pp. 233–266.

[9] M. Doi, *Molecular dynamics and rheological properties of concentrated solutions of rodlike polymers in isotropic and liquid crystalline phases*, J. Polym. Sci. Polym. Phys. Ed., 19 (1981), pp. 229–243.

[10] M. Doi and S. F. Edwards, *The Theory of Polymer Dynamics*, Oxford University Press, London, New York, 1986.

[11] A. Dutt, L. Greengard, and V. Rokhlin, *Spectral deferred correction methods for ordinary differential equations*, BIT, 40 (2000), pp. 241–266.

[12] J. Feng, G. Sgalari, and L. G. Leal, *A theory for flowing nematic polymers with orientational distortions*, J. Rheol., 44 (2000), pp. 1085–1101.

[13] J. Feng, J. Tao, and L. G. Leal, *Roll cells and disclinations in sheared polymer nematics*, J. Fluid Mech., 449 (2001), pp. 179–200.

[14] S. M. Fielding and P. D. Olmsted, *Kinetics of the shear banding instability in startup flows*, Phys. Rev. E (3), 68 (2003), 036313.

[15] S. M. Fielding and P. D. Olmsted, *Spatio-temporal oscillations and rheochaos in a simple model of shear banding*, Phys. Rev. Lett., 92 (2004), 084502.

[16] E. Fisher and P. T. Callaghan, *Shear banding and the isotropic-to-nematic transition in wormlike micelles*, Phys. Rev. E (3), 64 (2001), 011501.

[17] M. G. Forest, S. Sircar, Q. Wang, and R. Zhou, *Monodomain dynamics for rigid rod and platelet suspensions in strongly coupled coplanar linear flow and magnetic fields.* II: *Kinetic theory*, Phys. Fluids, 18 (2006), 103102.

[18] M. G. Forest and Q. Wang, *Monodomain response of finite-aspect-ratio macromolecules in shear and related linear flows*, Rheol. Acta, 42 (2003), pp. 20–46.

[19] M. G. Forest, Q. Wang, H. Zhou, and R. Zhou, *Structure scaling properties of confined*

Copyright © by SIAM. Unauthorized reproduction of this article is prohibited.

nematic polymers in plane Couette cells: The weak flow limit, J. Rheol., 48 (2004), pp. 175–192.

[20] M. G. Forest, Q. Wang, and R. Zhou, *The flow-phase diagram of Doi-Hess theory for sheared nematic polymers* II: *Finite shear rates*, Rheol. Acta, 44 (2004), pp. 80–93.

[21] M. G. Forest, Q. Wang, and R. Zhou, *The weak shear phase diagram for nematic polymers*, Rheol. Acta, 43 (2004), pp. 17–37.

[22] M. G. Forest, Q. Wang, and R. Zhou, *Monodomain dynamics for rigid rod and platelet suspensions in strongly coupled coplanar linear flow and magnetic fields*, Phys. Fluids, 51 (2007), pp. 1–21.

[23] M. G. Forest, Q. Wang, R. Zhou, and E. Choate, *Monodomain response of arbitrary aspect ratio nematic polymers in general linear planar flows*, J. Non-Newt. Fluid Mech., 118 (2004), pp. 17–31.

[24] M. G. Forest, R. Zhou, and Q. Wang, *Chaotic boundaries of nematic polymers in mixed shear and extensional flows*, Phys. Rev. Lett., 93 (2004), 088301.

[25] M. G. Forest, R. Zhou, and Q. Wang, *Kinetic structure simulations of nematic polymers in plane Couette cells.* II: *In-plane structure transitions*, Multiscale Model. Simul., 4 (2005), pp. 1280–1304.

[26] M. G. Forest, R. Zhou, and Q. Wang, *Nano-rod suspension flows: A* 2*d Smoluchowski-Navier-Stokes solver*, Int. J. Numer. Anal. Model., 4 (2007), pp. 478–488.

[27] A. Furukawa and A. Onuki, *Spatio-temporal structures in sheared polymer systems*, Phys. D, 205 (2005), pp. 195–206.

[28] C. Grand, J. Arrault, and M. E. Cates, *Slow transients and metastability in wormlike micelle rheology*, J. Phys. II, 7 (1997), pp. 1071–1086.

[29] F. Greco and R. Ball, *Shear-band formation in a non-Newtonian fluid model with a constitutive instability*, J. Non-Newt. Fluid Mech., 69 (1997), pp. 195–206.

[30] M. Grosso, R. Keunings, S. Crescitelli, and P. L. Maffettone, *Prediction of chaotic dynamics in sheared liquid crystalline polymers*, Phys. Rev. Lett., 86 (2001), pp. 3184–3187.

[31] T. Hagstrom and R. Zhou, *On the spectral deferred correction of splitting methods for initial value problems*, Commun. Appl. Math. Comput. Sci., 1 (2006), pp. 169–205.

[32] R. Hegger, H. Kantz, and T. Schreiber, *Practical implementation of nonlinear time series methods: The TISEAN package*, Chaos, 9 (1999), pp. 413–435.

[33] S. Heidenreich, P. Ilg, and S. Hess, *Robustness of the periodic and chaotic orientational behavior of tumbling nematic liquid crystals*, Phys. Rev. E (3), 73 (2006), 061710.

[34] C. Helzel and F. Otto, *Multiscale simulations for suspensions of rod-like molecules*, J. Comput. Phys., 216 (2006), pp. 52–75.

[35] S. Hess, *Fokker-Planck-equation approach to flow alignment in liquid crystals*, Z. Naturforsch., 31 (1976), pp. 1034–1037.

[36] W. Holmes, M. Lopez-Gonzalez, and P. Callaghan, *Fluctuations in shear banded flow seen by NMR velocimetry*, Europhys. Lett., 64 (2003), pp. 274–280.

[37] Y. T. Hu and A. Lips, *Kinetics and mechanism of shear banding in entangled micellar solutions*, J. Rheol., 49 (2005), pp. 1001–1027.

[38] R. Keunings, *Micro-macro methods for the multiscale simulation of viscoelastic flow using molecular models of kinetic theory*, in Rheology Reviews 2004, British Society of Rheology, Aberystwyth, Wales, 2004, pp. 67–98.

[39] D. H. Klein, C. Garcia-Cervera, H. D. Ceniceros, and L. G. Leal, *Computational studies of the shear flow behavior of a model for nematic liquid crystalline polymers*, ANZIAM J., 46 (2005), pp. C210–C244.

[40] M. Kröger, *Simple models for complex nonequilibrium fluids*, Phys. Rep., 390 (2004), pp. 453–551.

[41] M. Kröger and P. Ilg, *Deviation of Frank-Erickson elastic coefficients for polydomain nematics from mean-field molecular theory for anisotropic particles*, J. Chem. Phys., to appear.

[42] R. Kupferman, M. Kawaguchi, and M. M. Denn, *Emergence of structure in models of liquid crystalline polymers with elasticity*, J. Non-Newt. Fluid Mech., 91 (2000), pp. 255–271.

[43] R. G. Larson and D. W. Mead, *The Ericksen number and Deborah number cascades in sheared polymeric nematics*, Liquid Cryst., 15 (1993), pp. 151–169.

[44] S. Lerouge, J. P. Decruppe, and P. D. Olmsted, *Birefringence banding in a micellar solution or the complexity of heterogeneous flows*, Langmuir, 20 (2004), pp. 11355–11365.

[45] M. W. Liberatore, F. Nettesheim, N. J. Wagner, and L. Porcar, *Spatially resolved small-angle neutron scattering in the* 1-2 *plane: A study of shear-induced phase-separating wormlike micelles*, Phys. Rev. E (3), 73 (2006), 020504.

[46] M. W. Liberatore, F. Nettlesheim, E. W. Kaler, N. J. Wagner, T. Nu, and L. Por-

Copyright © by SIAM. Unauthorized reproduction of this article is prohibited.

CAR, *Characterization of Solutions of Wormlike Micelles under Flow: Microstructure and Investigations in the* 1-2 *Plane*, preprint, 2007.

[47] M. R. LOPEZ-GONZÁLES, W. M. HOLMES, P. T. CALLAGHAN, AND P. J. PHOTINOS, *Shear banding fluctuations and nematic order in wormlike micelles*, Phys. Rev. Lett., 93 (2004), 268302.

[48] G. MARRUCCI AND F. GRECO, *The elastic constants of Maier-Saupe rod-like molecular nematics*, Mol. Cryst. Liq. Cryst., 206 (1991), pp. 17–30.

[49] V. G. MAVRANTZAS AND A. N. BERIS, *Theoretical study of wall effects on rheology of dilute polymer solutions*, J. Rheol., 36 (1992), pp. 175–213.

[50] P. D. OLMSTED AND C.-Y. D. YU, *Phase separation of rigid-rod suspensions in shear flow*, Phys. Rev. E (3), 60 (1999), pp. 4397–4415.

[51] G. RIENÄCKER, M. KRÖGER, AND S. HESS, *Chaotic and regular shear-induced orientational dynamics of nematic liquid crystals*, Phys. A, 315 (2002), pp. 537–568.

[52] G. RIENÄCKER, M. KRÖGER, AND S. HESS, *Chaotic orientational behavior of a nematic liquid crystal subjected to a steady shear flow*, Phys. Rev. E (3), 66 (2002), 040702.

[53] G. SGALARI, G. L. LEAL, AND J. J. FENG, *The shear flow behavior of LCPs based on a generalized Doi model with distortional elasticity*, J. Non-Newt. Fluid Mech., 102 (2002), pp. 361–382.

[54] A. SONNET, A. KILIAN, AND S. HESS, *Alignment tensor versus director: Description of defects in nematic liquid crystals*, Phys. Rev. E (3), 52 (1995), pp. 718–722.

[55] Z. TAN AND G. C. BERRY, *Studies on the texture of nematic solutions of rodlike polymers.* 3. *Rheo-optical and rheological behavior in shear*, J. Rheol., 47 (2003), pp. 73–104.

[56] T. TSUJI AND A. D. REY, *Effect of long range order on sheared liquid crystalline polymers, part* 1: *Compatibility between tumbling behavior and fixed anchoring*, J. Non-Newt. Fluid Mech., 73 (1997), pp. 127–152.

[57] T. TSUJI AND A. D. REY, *Effect of long range order on sheared liquid crystalline materials: Flow regimes, transitions, and rheological phase diagrams*, Phys. Rev. E (3), 62 (2000), pp. 8141–8151.

[58] Q. WANG, *A hydrodynamic theory for solutions of nonhomogeneous nematic liquid crystalline polymers of different configuration*, J. Chem. Phys., 116 (2002), pp. 9120–9136.

[59] B. YESILATA, C. CLASEN, AND G. MCKINLEY, *Nonlinear shear and extensional flow dynamics of wormlike surfactant solutions*, J. Non-Newt. Fluid Mech., 133 (2006), pp. 73–90.

[60] H. YU AND P. ZHANG, *A kinetic-hydrodynamic simulation of microstructure of liquid crystal polymers in plane shear flow*, J. Non-Newt. Fluid Mech., 141 (2007), pp. 116–127.

[61] X. ZHENG, M. G. FOREST, Q. WANG, AND R. ZHOU, *Likelihood and expected-time statistics of monodomain attractors in sheared discotic and rod-like nematic polymers*, Rheol. Acta, 44 (2005), pp. 219–234.

[62] H. ZHOU AND M. G. FOREST, *Anchoring distortions coupled with plane Couette & Poiseuille flows of nematic polymers in viscous solvents: Morphology in molecular orientation, stress & flow*, Discrete Contin. Dyn. Syst. Ser. B, 6 (2006), pp. 407–425.

[63] H. ZHOU, M. G. FOREST, AND Q. WANG, *Anchoring-induced texture & shear banding of nematic polymers in shear cells*, Discrete Contin. Dyn. Syst. Ser. B, 8 (2007), pp. 707–733.

[64] R. ZHOU, M. G. FOREST, AND Q. WANG, *Kinetic structure simulations of nematic polymers in plane Couette cells.* I: *The algorithm and benchmarks*, Multiscale Model. Simul., 3 (2005), pp. 853–870.

Copyright © by SIAM. Unauthorized reproduction of this article is prohibited.